



HAL
open science

Neural network segmentation methods for fatigue crack images obtained with X-ray tomography

Ce Xiao, Jean-Yves Buffiere

► To cite this version:

Ce Xiao, Jean-Yves Buffiere. Neural network segmentation methods for fatigue crack images obtained with X-ray tomography. *Engineering Fracture Mechanics*, 2021, 252, 10.1016/j.engfracmech.2021.107823 . hal-03482906

HAL Id: hal-03482906

<https://hal.science/hal-03482906v1>

Submitted on 25 Jan 2022

HAL is a multi-disciplinary open access archive for the deposit and dissemination of scientific research documents, whether they are published or not. The documents may come from teaching and research institutions in France or abroad, or from public or private research centers.

L'archive ouverte pluridisciplinaire **HAL**, est destinée au dépôt et à la diffusion de documents scientifiques de niveau recherche, publiés ou non, émanant des établissements d'enseignement et de recherche français ou étrangers, des laboratoires publics ou privés.

Neural network segmentation methods for fatigue crack images obtained with X-ray tomography

XIAO Ce¹, BUFFIERE Jean-Yves^{1,*}

INSA LYON MATEIS

^a20 Avenue Albert Einstein, Villeurbanne

Abstract

Synchrotron X-ray tomography allows to observe fatigue crack propagation during *in situ* tests. Accurately segmenting the 3D shape of the cracks from the tomography image is essential for quantitative analysis. Fatigue cracks have small openings which result in low contrast images making crack segmentation difficult. Phase contrast available at synchrotron sources improves crack detection but it also increases the complexity of the image and human intervention is generally used to help traditional segmentation methods. In this work, an image segmentation method based on a convolutional neural network is developed to replace the user interpretation of images. Combined with a 'Hessian matrix' filter, this method can successfully extract 3D shapes of internal fatigue cracks in metals.

Keywords: synchrotron tomography, crack segmentation, convolutional neural network, fatigue

1. Introduction

X-ray Computed Tomography(CT) has become a well established characterization technique in materials science. It allows to observe defects (cracks, voids, inclusions) or phases in the interior of optically opaque samples with a

*Corresponding author

Email address: jean-yves.buffiere@insa-lyon.fr (BUFFIERE Jean-Yves)

URL: www.elsevier.com (XIAO Ce)

5 spatial resolution close to that of optical microscopy (*i.e.* in the micrometer range). Because of its non destructive character, tomography is often used to monitor the evolution of materials microstructure submitted to various experimental conditions during *in situ* tests [1]. For example 3D images of damage development in metallic samples during monotonic cyclic tests [2] [3], in Al alloys [4], steels [5], Ti alloys [6], Mg alloys [7] have been published. A detailed review can be found in [8]. With the development of faster detectors and more brilliant sources, during one single test at a synchrotron facility, several tens of 3D images can be recorded. The quantitative analysis of such large data sets must be carried out by automatic or semi automatic image analysis of binary images obtained by segmentation. This step is crucial in the data processing chain; it must extract the phenomenon of study (cracks or pores formation under mechanical loading, cell swelling or collapsing in a foam, phase coarsening during heat treatment, particle tracking ...) from a gray scale image and turn it into binary data.

20 A range of thresholding methods can be found in the literature: classic gray level threshold methods [9] combined with morphological operations [10] [11], feature extraction methods [12] [13], machine learning methods [14][15], neural network methods [16] [17].

Thresholding the gray level histogram is the simplest and most widely used method for image segmentation, but it is highly sensitive to noise and artifacts and thus not very efficient in the vicinity of the crack tip where the crack opening is low, even if the sample is under load. Feature extraction methods, including Hough transform [18], finite plane integral transform [19] or filtering based on Hessian matrix [20], assume that the crack has a prescribed shape in the image such as a line (in 2D) or a plane or a portion of plane (in 3D). Such methods have been used for example in the case of bones [12] or concrete [21] for which crack opening can be very small (lower than 1 μm). More recently, with the development of machine learning algorithms, the random forest method [15] or the convolutional neural network method [17] have been developed for image segmentation. The basic ideas of those methods is to 'train' the segmentation

algorithm on a set of manually segmented images (the ground truth). Recent results on high resolution synchrotron images of Al alloys show that by using such methods the total time required for segmentation is much lower than that required by manual segmentation [22]. To the best of our knowledge, such
40 methods have not yet been applied for fatigue crack segmentation.

Fatigue cracks in the interior of metals can be observed by laboratory tomography or by synchrotron tomography. The challenges for segmenting the cracks are different for the those two types of CT images. For the former, the limited x-ray energy and signal-to-noise ratio give low contrast and relatively noisy gray
45 scale images (Figure 1.a and b). In synchrotron images, phase contrast helps for detecting the cracks, but the interpretation of the gray-level is more complicated: because of diffraction effects the same crack can appear black or dark in the reconstructed image depending on its opening. This type of contrast, which will be described in more details in section 3 of the paper, poses a number of
50 challenges for automatic segmentation methods which have to be carried out at least partially manually. In this paper we propose to use deep learning methods to reproduce the user intervention for obtaining continuous, complete, and physically meaningful 3D cracks.

The paper is organised as follows: first a segmentation method based on
55 the application of Hessian Matrix is described. This method which is very efficient for extracting planar features within noisy images (like lab tomography images) is presented. Then a method based on a deep learning algorithm has been used to threshold cracks in synchrotron CT images. The trained model is used to segment successive images of the same specimen obtained during an
60 *in situ* fatigue test at different number of fatigue cycles showing the efficiency of the method. The effect of the input Ground Truth on the segmentation results is then discussed using an image with a larger voxel size and different reconstruction parameters.

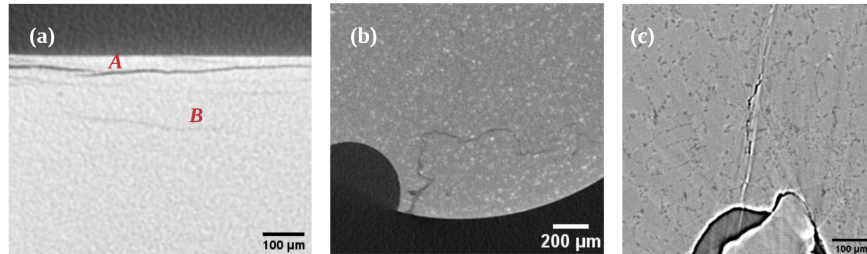


Figure 1: Reconstructed images of fatigue cracks obtained by laboratory (a)-(b) and synchrotron x ray Tomography(c). Lab tomography: (a) Bearing steel after Rolling Contact Fatigue Test, voxel=2.1 μm , Accel voltage 160 kV. Cracks connected to the sample surface (detail A) appear with a better contrast than internal crack (detail B) because of lower opening; (b) Al alloy sample, voxel size =size =2.5 μm , Accel voltage 160 kV; Synchrotron tomography: (c) Al alloy sample, voxel size =1.3 μm , Beam energy 29keV, the distance between the detector and the object: 15cm.

2. Methodology

65 2.1. Hessian matrix-based method

As shown in Figure 2g, the method consists of three steps:

Step 1 subtraction filter

A smoothed image (3D median filter) of the crack is subtracted from the original image bringing the crack in the foreground and reducing the noise level. (Figure 2b). The value used for the window size for the median filter (11 voxels)
 70 (Figure 2b). The value used for the window size for the median filter (11 voxels) is a compromise between a value small enough to reduce the processing time and large enough to remove the crack from the matrix [23].

Step 2 Crack contrast enhancement

Inspired from a method developed for segmenting micro-cracks in bones [12],
 75 a combination of linear bilateral, steerable and nonlinear bilateral filters (sub step i to k) is used for increasing the contrast and denoising the crack image.

- Substep i: Linear bilateral filter

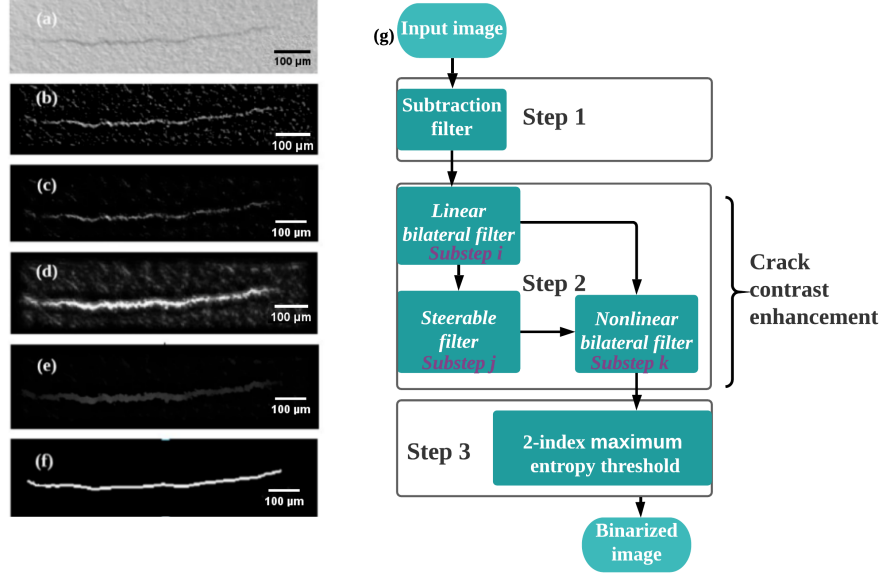


Figure 2: Algorithm flow chart of the Hessian matrix-based method: (a) 2D slice of a laboratory tomography image from a bearing steel sample containing a crack (b) Output of optimized subtraction filter (c) Output of linear bilateral filter (d) Output of steerable filter (e) Output of nonlinear bilateral filter (f) Binarized image (g) algorithm flow chart of the method.

Before calculating the Hessian matrix, it is necessary to smooth the image to perform second order derivation operations. To do so, a bilateral 3D Gaussian
 80 filter [24] is used; it allows to remove noise in the image while preserving the edges of the cracks. The equation of this filter is written:

$$\begin{aligned}
 F(X) &= \frac{1}{\mu} \int f(X) e^{-\frac{1}{2} \left(\frac{\|Y-X\|}{\sigma_{d1}} \right)^2} e^{-\frac{1}{2} \left(\frac{\|f(Y)-f(X)\|}{\sigma_{d2}} \right)^2} dx \\
 \text{with } \mu &= \int e^{-\frac{1}{2} \left(\frac{\|Y-X\|}{\sigma_{d1}} \right)^2} e^{-\frac{1}{2} \cdot \frac{\|f(Y)-f(X)\|}{\sigma_{d2}}^2} dx
 \end{aligned} \tag{1}$$

Where $X(x,y,z)$ and $Y(x,y,z)$ are the coordinates of a given pixel and its neighbors, respectively, $f(X)$ is the gray value of the input image (output of subtraction filter). σ_{d1} and σ_{d2} are the scale constants of the Gaussian distribution
 85 (values corresponding to the different volumes investigated are given in A.1).

- Substep j: Steerable filter

To optimally enhance the contrast of cracks in the reconstructed volumes, the 3D steerable filter based on the Hessian matrix proposed by F.Aguet [25] is used. Some examples of Hessian matrix based methods for crack segmentation
90 can be found in the literature. For example, low contrast micro-cracks in human bones have been detected with this approach by A.Larrue *et al.*. Although in this case the cracks were investigated by synchrotron tomography they present some similarities with those shown in Figure 2.a like a low contrast due to low opening [12][13]. Using the same idea, C.Chateau has used the eigenvalues of
95 the Hessian matrix to construct a contrast-enhancing filter to segment cracks in lightweight concrete; in that specific case the segmented cracks correspond to the residuals of a Digital Volume Correlation calculation [21]. The basis of the Hessian matrix based method is briefly summarised hereafter, more details can be found for example in [20].

100 The eigenvalues of a Hessian matrix calculated for each pixel of an image represent the anisotropy of the variation of the gray value along the direction of the corresponding vector. According to this, steerable filters can be designed for different features detection, and here we use the planar detector [25]. For a voxel belonging to a locally planar feature, the eigenvalues of the Hessian matrix
105 should be larger in one direction (the normal of the plane) and smaller in the remaining two directions. It is assumed that the shape of fatigue cracks correspond to a series of adjacent planar portions of various sizes. The eigenvalues of the 3D Hessian matrix are calculated at each voxel and its the maximum value is assigned to the voxel.

110 - Substep k Nonlinear bilateral filter

The output image of the steerable filter contains a lot of noise (see Figure 2d) as the crack is not the only planar structure detected (Figure 2d). To keep only those voxels belonging to the crack, a nonlinear bilateral filter [26] is used; it combines the output of the steerable filter (substep i) and that of the linear

115 bilateral filter (substep j); it is written:

$$\begin{aligned}
 F(X) &= \frac{1}{\mu} \int f(X) e^{-\frac{1}{2} \left(\frac{\|Y-X\|}{\sigma_{d1}} \right)^2} e^{-\frac{1}{2} \left(\frac{\|S(Y)-S(X)\|}{\sigma_{d2}} \right)^2} dx \\
 \text{with } \mu &= \int e^{-\frac{1}{2} \left(\frac{\|Y-X\|}{\sigma_{d1}} \right)^2} e^{-\frac{1}{2} \left(\frac{\|S(Y)-S(X)\|}{\sigma_{d2}} \right)^2} dx
 \end{aligned} \tag{2}$$

Where $X(x,y,z)$ and $Y(x,y,z)$ are the coordinates of a given pixel and its neighbors, respectively, $f(X)$ is the gray value of the input image (result of the linear bilateral filter), $S(X)$ is the value of the output image of the steerable filter. σ_{d1} and σ_{d2} are scale constants of the Gaussian distribution. The term non-
 120 linear means that in this bilateral noise filtering process, the output of the linear bilateral filter $f(X)$, is different from the image ($S(X)$, the output of the steerable filter) which is used to calculate the parameters of the filtered convolution kernel. The results of this last filtering step shown in Figure 2.e.

Step 3 Double index maximum entropy threshold

125 To eventually obtain the binary image of the crack after those filtering steps the ‘two-index entropy threshold’ introduced by Bhowmik *et al.* [10] is used (equation 3). The first index is the gray value of a single-pixel and the second one is the average gray value in the neighborhood. In our case the first index is the average gray value in the in-layer neighborhood(3*3). The second indicator
 130 $g(x,y,z)$ correspond to the continuity between two adjacent layers (equation 3). For a given voxel, $g(x,y,z)$ counts how many voxels (ignoring those at the edge of the image) have close gray value and eigenvectors (computed in the Steerable filter) within a radius w of the two adjacent layers (e.g. $w=1$, represents a 3*3 windows centered on the considered voxel in the two adjacent layers). The two
 135 threshold values for each slice are chosen to maximize the information entropy

of each slice.

$$\begin{aligned}
 g(x, y, z) &= \sum_{i, j=-w}^w \delta(x + i, y + j, z \pm 1) \\
 \delta(x + i, y + j, z \pm 1) &= \begin{cases} 1, & \text{if } \frac{|f(x, y, z) - f(x + i, y + j, z \pm 1)|}{f(x, y, z)} < \alpha \\ & \text{and } |d(x, y, z) - d(x + i, y + j, z \pm 1)| < \beta \\ 0, & \text{else} \end{cases}
 \end{aligned} \tag{3}$$

$f(x, y, z)$ is the output of the non linear filter, $d(x, y, z)$ is the eigenvector of the Hessian matrix calculated in the steerable filter. α and β are two parameters which are tuned to achieve crack continuity (see appendix A).

140 2.2. Deep learning thresholding method for synchrotron CT images

The global approach is divided into three steps: first, a 2D deep learning method(U-net) provides a probability maps; second, the method described in section 2.1 extracts the crack from the probability maps; third, the crack tip is smoothed method (Alphashape method). The flowchart of the algorithm is shown in Figure 3.

2.2.1. U-net

In the last years, several deep learning methods have been proposed for image classification and recognition (e.g. ImageNet, AlexNet ...) see [17] for a review. In this work we use a convolutional neural networks (CNN) called U-net, following the approach of Strohmann *et al.* [22] who also used this type of algorithm for segmentation of the microstructural components of an Al-Si alloy within a high resolution synchrotron tomography image.

The network(U-net) structure used here is shown in Figure 4. The encoder procedure Step 1-4 aims at identifying features at different scales by a series of convolution (Conv2D) and downsampling operations (Maxpooling2D). After each step, the image size is halved and the feature maps number is doubled. The purpose of the decoder Step 6-9 is to restore the feature image to its original resolution by Convolution (Conv2D) and upsampling operation (Bilinear interpolation). After each step in decoder, the image size is doubled and the feature

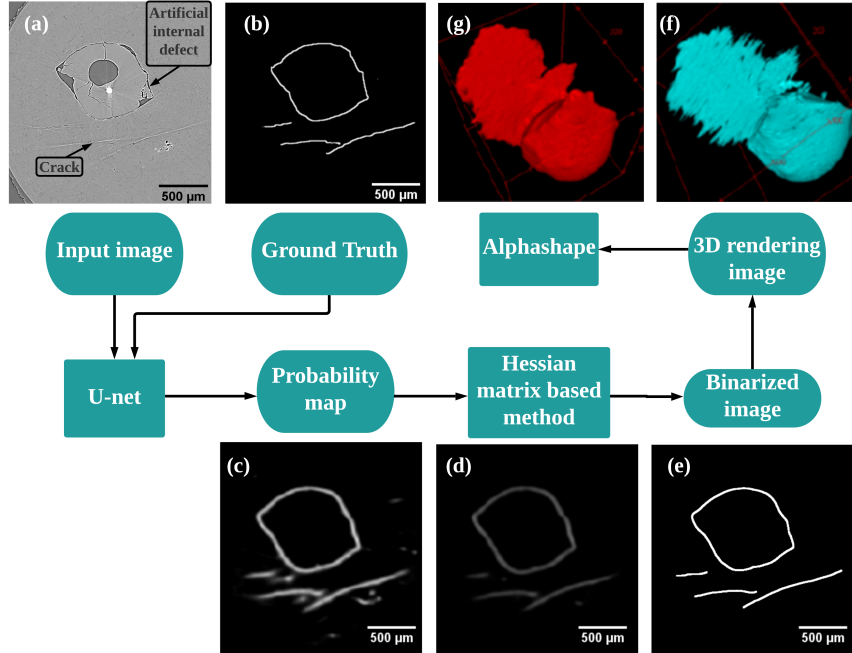


Figure 3: Flowchart of the segmentation algorithm for synchrotron images. (a) 2D slice of a synchrotron tomography image of a cast Al sample showing a crack (bottom arrow) and an internal artificial defect (upper arrow), the crack also appears in Figure 6 with an improved visibility; (b) Manually segmented image of (a) used as Ground Truth for training the U-net network; (c) Probability map of (a); (d) Enhanced and denoised image obtained with the Hessian matrix method; (e) Binarized image of (d); (f) 3D rendering image of (e); (g) 3D rendering image with smoothed crack tip by Alphashape.

160 maps number is halved. Each output of the decoder is concatenated with the output of the encoder with the same dimension. A more detailed presentation of the U-net method can be found for example in [17]. The details of each step to reconstruct the Neural work can be found in Table B.2 and the basic explanation of the operations used here can be found in Table B.3.

165 As shown in the top part of Figure 4, the training process of the network consists first in generating a binary image with randomly initialized kernel values. From this image and the ground truth, a loss is calculated (loss function:

binary cross entropy), from which updated kernel values are generated. With those values a second iteration can start. The process is repeated for a given
170 number of iterations.

The ground truth was obtained by manually segmenting some slices using the pixel brush tool in matlab ¹. The time to manually segment a 512*512 pixel image containing a crack is about 2 minutes (total time for 80 slices: approximately 3hours). In order to avoid over-fitting, ‘data augmentation’ is
175 performed on the training data by using gray scale and manually segmented images rotated at a random angle.

The training and testing of Unet was implemented in Python 3.0 (Tensorflow Keras), using Adam optimizer (learning rate=0.0005) and ‘binary-cross-entropy’ as a loss function. Training was carried out for 100 epochs each with 50 images
180 batch. The total training time of the Unet (input image size= 512*512) for each epochs is about 10 minutes on a standard PC with 16 GB DDR3 memory and Intel(R) i5 Core 1.9 GHz² (total time for 100 epochs 16h).

2.2.2. Hessian matrix based filter and Two-index entropy threshold

The output of the above described method is a 3D probability map (values
185 between 0 and 1). Such maps can be transformed into binary data by using a threshold [22]. Instead, in order to reinforce the crack 3D continuity we have used the method described in section 2.1: the ‘Hessian matrix based filter’ is used first to detect planar structures belonging to the crack, the output is thresholded using the ‘2-index entropy threshold’.

190 2.2.3. AlphaShape

The relatively jagged crack tip obtained after thresholding (Figure 3.e) is finally smoothed as suggested by Lou *et al.* [27] who used the ‘3D AlphaShape’ algorithm initially proposed by H.Edelsbrunner and E.P.Mucke [28].

¹Image Labeler plugin in Matlab 2018

²This machine has been used for all calculations reported in this work

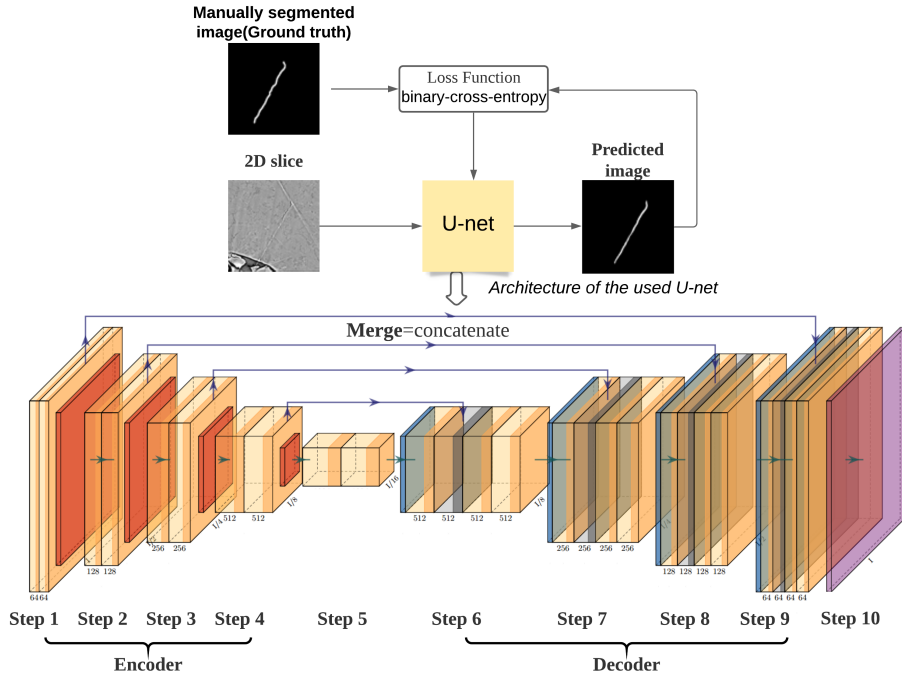


Figure 4: Schematic explanation of the U-net training process and visualization of the network structure. The details of each step to reconstruct the Neural work can be found in Table B.2

3. Results and discussion

195 3.1. Segmentation of crack images obtained by laboratory CT

In principle Laboratory CT machines can reach voxel sizes which are comparable to those of synchrotron tomography. In practice, however, lab sources suffer from i) a lower signal/noise ratio and ii) a non coherent x-ray beam (much less coherent than that at a synchrotron source). The coherence produces phase
 200 contrast which helps to detect sub voxel features [29]. Internal fatigue cracks visible on Figure 1a have a lower opening than surface ones. As shown in Figure 1a, the most visible cracks are those connected to the surface; cracks in the bulk appear with a much lower contrast and are hardly visible on the raw image. Such internal cracks represent a big challenge for thresholding. In Figure 1.a,
 205 the voxel size is 2.1 μm . A lower voxel size could deliver a better image as shown

in [30] with a $0.7\ \mu\text{m}$ voxel size also on rolling contact fatigue cracks in steels³. However such small voxel sizes have at least two drawbacks. First, the sample dimensions are reduced [31] and, second, large exposure times are required. In the above mentioned paper Danielsen *et al.* [30] mention an exposure time
210 between 10 and 20s resulting in scanning times larger than 10h [32]. Such long scans cannot be used for *in situ* experiments. For those reasons one has very often to bear with larger voxel sizes and/or shorter scans.

The result of the classical crack segmentation method on the internal crack of Figure 1 is shown on Figure 5.b; the thresholding process is as follows: i)
215 contrast enhancement by brightness adjustment, ii) 3D Gaussian filtering denoising iii) segmentation by using a threshold value on the grayscale histogram. As can be seen on the figure, the crack with low contrast has not been properly detected. In the 3D rendering some parts of the crack are missing making quantitative analysis very difficult. Figure 5 shows the results obtained on the
220 same crack by the Hessian matrix method described in section 2.1. A much more continuous crack is obtained even in crack sections with very low opening. Another example is given in Appendix C on an Al sample. In both cases, the proposed algorithm performs well compared to single value gray level histogram threshold providing a much more continuous crack surface. It is likely, however,
225 that the real crack tip will remain undetected given the voxel size used⁴ but one can assume that the error remains constant along the crack front allowing to capture the *shape* of the cracks with a reasonable accuracy. As explained in section 1, being able to extract automatically crack fronts is a key issue for *in situ* experiments where many successive crack fronts are recorded on a single
230 sample. The proposed algorithm can also help for thresholding cracks imaged by synchrotron tomography as explained in the next section.

³in that specific case the authors have also used different threshold values depending on the crack thickness. Those values were defined manually.

⁴As a rule of thumb the spatial resolution is of the order of twice the voxel size

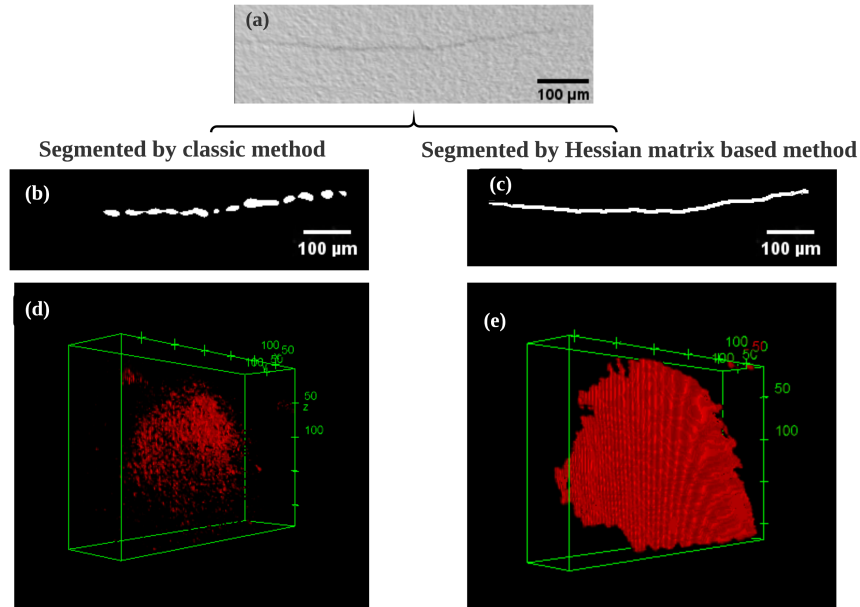


Figure 5: Segmentation of a rolling contact fatigue crack obtained by laboratory CT. (a) Reconstructed slice in the raw image (voxel size = $2.1 \mu\text{m}$) (b) and (d) Segmented slice and 3D rendering obtained by classical gray level histogram threshold (c) and (e) Segmented slice and 3D rendering obtained by the Hessian matrix-based method. The Hessian matrix improves the continuity of the binary crack in spite of its low contrast and opening.

3.2. Segmentation of crack images obtained by synchrotron tomography

3.2.1. Limits of the Hessian matrix based method

3D images of fatigue cracks have been recorded by synchrotron tomography
 235 in a cast Al sample during a series of *in situ* ultrasonic fatigue experiments [33].
 The tests were carried out at PISCHE beamline of synchrotron SOLEIL, the
 energy of the beam (filtered white beam) is 29keV the voxel size $1.3 \mu\text{m}$. Figure 6
 shows an image of one specimen after 1.91×10^7 cycles. The fatigue specimen
 contains an internal artificial defect (partly visible on the bottom left of the
 240 figure) in order to foster internal crack initiation.

The Hessian matrix method described in section 1 was used to segment
 the crack observed in this sample. The result, shown in Figure 6.c is that

this method fails at producing a continuous crack. This is because the contrast created by the crack in the reconstructed image is different from that obtained
245 in laboratory CT. Because of the spatial coherence of the beam, some phase contrast appears at the crack surface.

More precisely, as shown in Figure 6.a, three different type of contrast (or gray levels) can be observed:

- black (type 1 on Figure 3.a) for voxels belonging to a crack part with
250 opening larger than 1 voxel (attenuation contrast);
- white (type 2 on Figure 3.a) for voxels belonging to a crack part with sub voxel opening (phase contrast);
- white (type 3 on Figure 3.a) for voxels belonging to a streak artifact;

Cracks which propagate in metals from internal defects grow in an environ-
255 ment which is not the ambient air. As a result the crack surfaces are extremely flat because they correspond to crystallographic planes [34]. The alloy studied here being a foundry alloy, the grain size is of the order of 600 μm so that those flat surfaces can extend over several hundreds of micrometers. This creates some streak artifacts, mostly at the end of the cracks, where they seem
260 to extend the crack plane (Type 3 defect in Figure 6.a). Those artifacts are known in synchrotron tomography although their exact origin remains unclear. F.P.Vidal *et al.* have discussed the origin of similar streak artifact in 3D images of Ti/SiC fibre composites. For the authors, the existence of artifacts may be due to the detector impulse response [35]. The same conclusions are given by
265 L.Croton *et al.* from simulation of phase contrast synchrotron tomography of the human brain [36]. C. Madonna *et al.* found similar streak artifact in synchrotron tomography images of rock. According to these authors, they are due to exponential edge-gradient effects [37]. Without a better understanding of the origin of such artifact it is not possible, yet, to suppress them from reconstructed
270 images and one has to adapt the segmentation methods to their presence.

In practice, the only way to distinguish real cracks from artifacts relies on the user judgement during thresholding, based on what can be expected from the crack in terms of propagation direction. That is, cracks should start from the internal defect, and grow towards the sample surface. Also, the crack opening
275 should decrease from the crack mouth (at the internal defect) to the tip.

When some black segments are present in the image (Figure 6b) one can reasonably assume that a crack is present; often those segments are joined by white ones (Figure 6b) and the crack position corresponds to the union of those segments. When the crack opening is too small, it appears as a white line ('Type
280 2'). Instead, the part marked 'Type 3', is judged as a strike 'artifact'.

Because both strike artifacts and partially opened cracks appear in white it is not possible to extract them simply based on their gray levels. It is the user who decides which is which based on his/her experience and also by looking at the crack shape/position in neighbouring slices or on slices with a different
285 orientation (e.g. orthogonal views like those labeled 'sectional view' on Figure 6). Needless to say that such a process is long (approximately 2 minutes per slice), tedious, prone to errors and almost impossible to carry on more than a few volumes. Typically however the quantitative analysis of an *in situ* fatigue test might require thresholding tens of such 3D images. To try to solve this
290 problem which is a true bottleneck in data analysis, we have used the deep learning algorithm presented in section 2.2. The results obtained are presented in the following section.

3.2.2. Application of deep learning based method to fatigue crack in synchrotron tomography volume

295 The deep learning algorithm is used to segment the volume shown in Figure 6. As explained in section 2.2.1, 80 slices (out of 1200 for the whole image) were manually segmented (70 for training and 10 for validation). To reduce the computation time, the original image (1200*1200) is resized to 512*512 pixels before training the network.

300 The 3D probability map obtained from the whole block by the U-net algo-

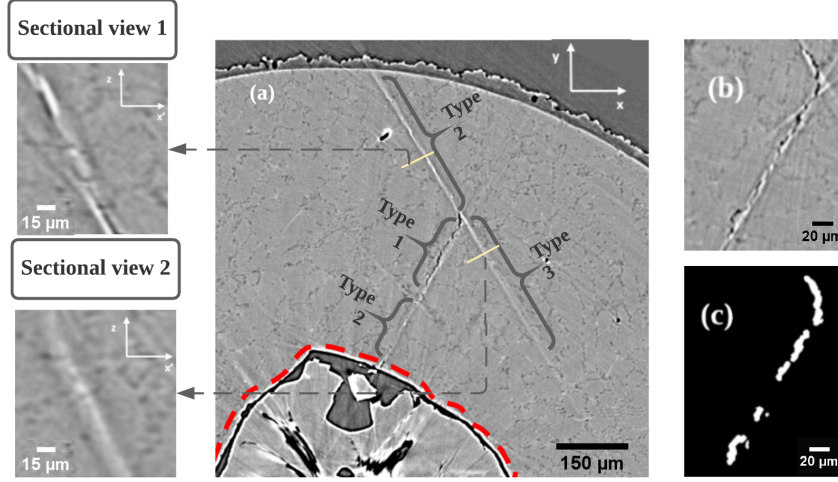


Figure 6: (a) 2D slice of a synchrotron tomography image of a cast Al sample showing an internal fatigue crack initiated from an artificial defects (underlined by a dashed red line) after 1.91×10^7 cycles (voxel size $1.3 \mu\text{m}$). Three types of contrast are observed: 1.crack with opening of the order or larger than 1 voxel (black); 2.crack with subvoxel opening (white); 3.streak artifact (white). (b) and (c) thresholding of the crack using the Hessian matrix method described in section 2.1.

rithm has been first binarized using a threshold of 0.5. The result is shown in Figure 7e and f and compared with the results obtained with the Hessian matrix approach (Figure 7b and c). If the Unet network is more successful at thresholding the crack, some discontinuities remain. In particular, the part of the crack close to the internal defect surface is missing. Changing the threshold to a lower value enables to detect that part but a lot of noise appears in the map. Improving the accuracy of the probability map would require more labor cost (see next section). In addition, this method is a slice by slice 2D approach that does not take advantage of the 3D information of the crack image. As a result, as explained in section 2.2 we have used the Hessian based algorithm developed for lab CT images to obtain a binary image from the probability map. The result is shown in Figure 7g and h; the crack appears much more continuous and the missing part connecting the internal defect is now visible. This is obtained

thanks to i) the Hessian matrix method which reinforces the contrast of planar
 315 features and ii) the 2-index max entropy threshold which takes advantage of the
 3D information in the probability map.

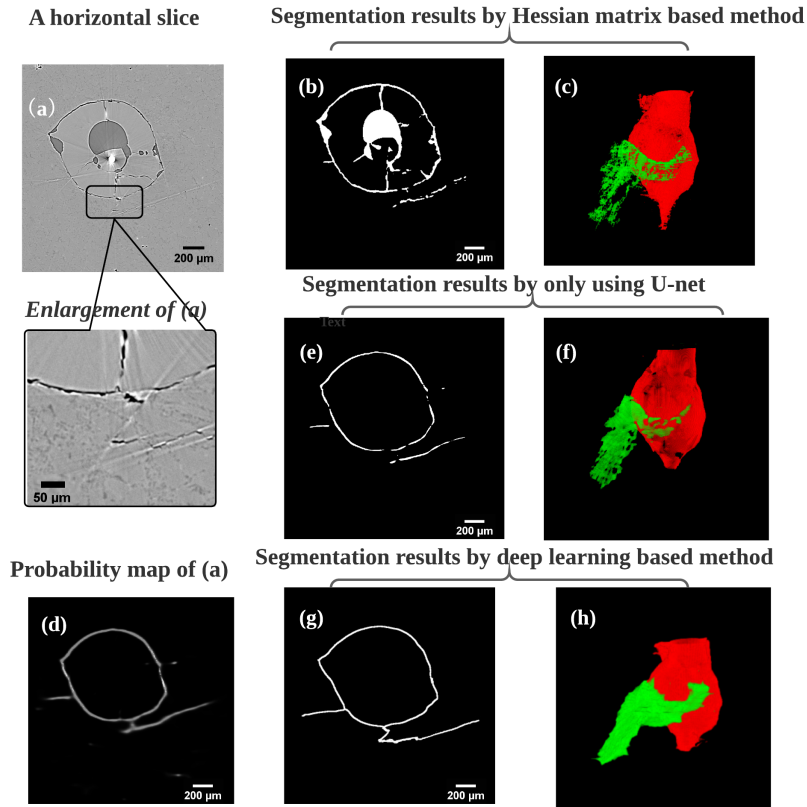


Figure 7: Results of different segmentation methods: volume obtained at PISCHE beamline of synchrotron SOLEIL: energy=29keV, distance between specimen and detector=15cm, voxel size=1.3 μm, crack observed after 1.91×10^7 cycles. (a) 2D horizontal slice; (b)~(c) 2D segmented slice and 3D rendering by ‘the Hessian matrix based method; (d) Probability map of (a); (e)~(f) the 2D segmented slice and 3D rendering by only using U-net; (g)~(h) 2D segmented slice and 3D rendering by deep learning based method.

3.2.3. *Application: segmentation of a series of synchrotron tomography volumes obtained during an in situ test*

For illustrating the ability of the trained algorithm to process series of dataset
320 automatically, we have used two volumes of the same sample reconstructed after
 1.84×10^7 and 1.98×10^7 fatigue cycles [33]. Those volumes were segmented
by the U-net model trained on a third volume as explained above. The seg-
mentation of the two new volumes using the trained network is relatively fast:
20 minutes on the computer mentioned above. The results are shown in Fig-
325 ure 8. In spite of the complex contrast visible on the 2D graylevel slices, the
proposed method allows to obtain complete images of the two successive crack
positions (shown in blue and yellow). After registration of the reconstructed
volumes using the defect, the two reconstructed cracks superimpose satisfacto-
rily and, interestingly, one can see that the propagation of the crack detected at
330 1.84×10^7 cycles is not uniform but a part of its front is arrested. Such crack
arrests have been rarely reported in 3D; they can only be observed if the num-
ber of tomographic scans is large enough which results, as explained, in large
series of dataset which must be systematically analysed. As mentioned before,
it is unlikely that the thresholding process can detect the "real" crack front,
335 nevertheless assuming that the error is roughly constant along the crack front
(same opening level) a systematic thresholding/processing, even imperfect, can
help to detect interesting regions of the crack or cycling steps which can be
analysed with more details if necessary (for example using gray level 2D slices).
The proposed segmentation method delivers *continuous* crack surfaces, which
340 can be transformed into meshes for finite element calculations without further
treatment.

As a final remark, in the proposed approach, each segmented 3D image
of a crack is independent of the previous or the next 3D image in the series,
although a clear continuity exist between them. Some deep learning algorithms
345 (Recurrent Neural Network - RNN or Long Short Term Memory-LSTM) have
been suggested for taking into account the continuity between different data-

sets in the field of 3D biomedical imaging [38] or in the prediction of gradual ocular disease [39]. This type of algorithms could be used to ensure a better compatibility between the different 3D images in the temporal sequence and produce more reliable results on crack growth.

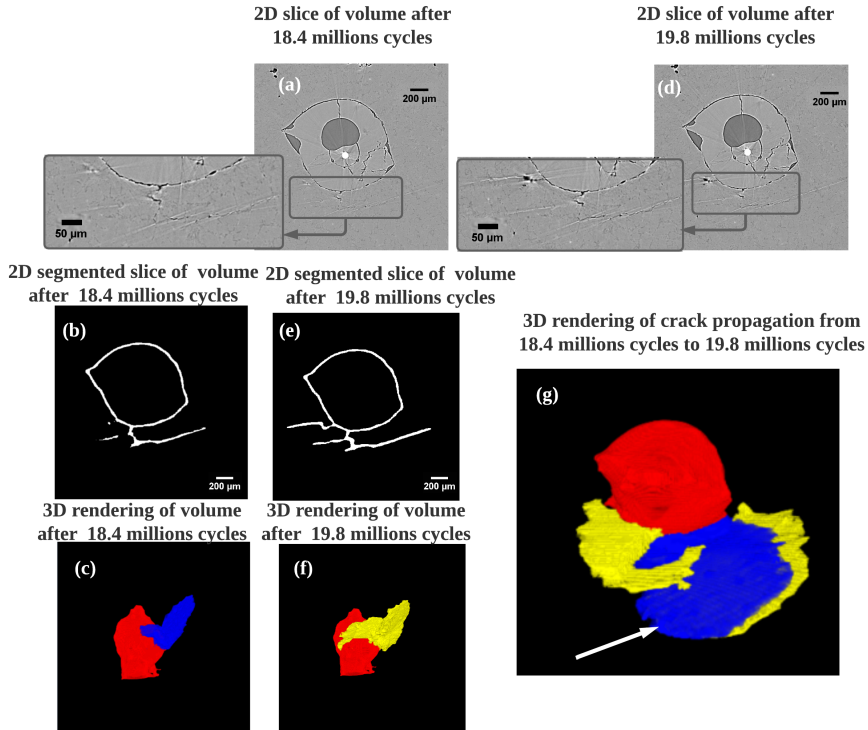


Figure 8: Segmentation results obtained with the trained U-net model for two successive volumes of an Al samples after 1.84×10^7 cycles (a,b,c) and 1.98×10^7 cycles (d,e,f). The U-net is trained on a third volume at a different number of cycles. The systematic analysis enabled by the algorithm of the successive volumes reveals a crack arrest on a region of the crack front (see arrow on g).

3.2.4. Influence of reconstruction parameters

If the reconstruction of 3D images always use the Filtered Back Projection algorithm, the contrast obtained in the raw images that are to be segmented varies from one synchrotron source to the other because the beam coherence,

355 the type and quality of optics, detector and scintillators vary. We have therefore
tested the applicability of our segmentation method on a dataset different from
the one described above. The material used is the same (cast Al alloy) and
the experiments are also similar (same in situ rig and cycling conditions). The
images have been recorded at the SYRMEP beamline of Elettra synchrotron in
360 Trieste. The Energy of the beam (29keV) and the specimen to detector distance
(15cm) are the same as in SOLEIL but the voxel size is different (2.2 μ m) and
the Paganin method [40] for phase retrieval was used during reconstruction. As
shown in Figure 9.a, the contrast of the cracks is different from that observed in
Figure 6 or 7 (cracks with low openings tend to appear with white contrast only)
365 in part due to the Paganin filter which reduces the spatial resolution because it
acts as a low-pass filter [41]. Distinguishing the cracks from the strike artifacts
becomes more difficult even with the eye.

First, the U-net network was trained with 70 manually segmented slices
(learning rate, type of loss function and other parameters are the same as in
370 section 3.2.1). After 100 epochs (50 images batch), the probability maps ob-
tained are shown in Figure 9.b. Compared with the probability map observed
in Figure 7, overall, the cracks show a lower contrast and some parts are not
detected (e.g. the part labeled Part A in Ground Truth Figure 9.d). The 3D
rendering shown in Figure 9.c., shows that some parts of the cracks close to
375 the internal defect are completely missed during segmentation (see arrow on
figure). To improve crack detection, the number of manually segmented images
was doubled (140 images). By doing so, Part A was detected in the probability
maps (Figure 9.e), but with a low contrast and, as a result, this part of the
crack is still not completely imaged in the 3D rendering. By looking closely
380 at the shape of Part A it was noticed that it is a crack which grows from the
defect perpendicular to the stress direction (mode I) which is also the rotation
axis during the tomography experiment. Thus Part A only appears on a few
(approximately ten) of the horizontal slices (perpendicular to the rotation axis)
used for training the model. In practice, for manually thresholding that part
385 of the crack, the user would use the 3D information by looking at slices with

different orientation to confirm (or infirm) his/her interpretation.

In slices containing the rotation axis mode I cracks such as part A are indeed more clearly observed (Figure 9.g). Therefore, 70 vertical slices of the same volume were used to train the network. (Figure 9.j). By comparing Figure 9j
390 and h one can clearly see that the probability map is much closer to Ground Truth than when horizontal slices were used (compare with Figure 9d and e). The new 3D rendering produced with the vertical slices (Figure 9.i), now shows a more complete crack, with a fully detected Part A.

From the above results, we can conclude that the network should be trained
395 in the most favourable configuration, i.e. using slices where the cracks are the most evident to visualise by eye. From that point of view, however, the cracks investigated here form a special case as they are very planar (crystallographic) and strongly inclined with respect to the stress direction. Such cracks are therefore well detected/visible on slices perpendicular to the rotation axis. However,
400 in a more general case, cracks initiated from a surface during uni-axial tension-compression tests would generally grow in mode I and therefore it is advised to train the model on slices containing the rotation axis. It also seems that the use of a slightly larger voxel (allowing larger samples to be imaged) and a limited loss of spatial resolution can be compensated by an increase in the number of
405 slices used to train the network but more data would be required to confirm that point. Similarly, the parameters of the neural network training (learning rate/type of loss function /network structure, etc.) will also affect the segmentation results. For example, changing the type of loss function has been shown to improve the segmentation quality of different phases in synchrotron CT images
410 of an Al alloy [22]. These parameters can be seen more as a talent of the neural network learning. In this work, we focused more on the effect of different user mind inputs on the same neural network. Some results obtained with different loss function type and learning rate are shown in Appendix D.

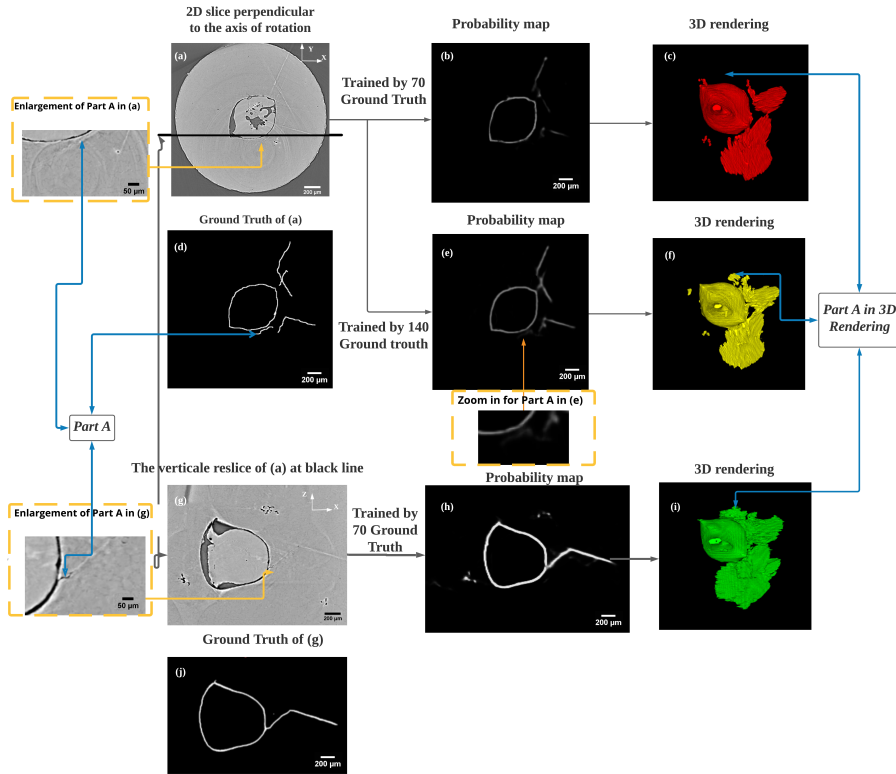


Figure 9: Effect of different inputs on deep learning based method segmentation results (volume obtained at Elettra Synchrotron: energy=29keV ,distance between specimen and detector=15cm, voxel size =2.2 μ m reconstruction with FBP and Paganin). (a) 2D slice perpendicular to the rotation axis (*horizontal* slice); (b)'Probability map' obtained with 70 horizontal Ground Truth slices; (c) 3D rendering obtained with network trained using 70 horizontal Ground Truth slices; (d) Ground Truth of (a); (e) 'Probability map' obtained with 140 horizontal Ground Truth slices; (f) 3D rendering obtained with network trained using 140 horizontal Ground Truth slices; (g) 2D slice parallel to the rotation axis (*vertical* slice) corresponding to the black line shown in (a); (h) 'Probability map' obtained with 70 vertical Ground Truth slices; (i) 3D rendering obtained with network trained using 140 vertical Ground Truth slices (j) Ground Truth of (g). In (i) a more complete crack is obtained.

4. Conclusion

415 With the development of fast tomography at synchrotrons facilities, scans typically last less than 5 minutes. As a result, *in situ* experiments monitored by

tomography can generate a considerable amount of data. In the processing of such data, thresholding is a bottleneck on which relies the efficiency and quality of quantitative analysis. In this paper we have described several methods for the thresholding of fatigue cracks in tomographic volumes. In a reconstructed 3D image, such cracks can be quite difficult to threshold when their opening is low, particularly in the case of laboratory tomography.

The first method described in this paper for thresholding fatigue cracks in lab CT relies on and merges several approaches developed for bones or concrete. A Hessian matrix approach coupled with a series of bilinear filters are used to detect flat features which connectivity in 3D is reinforced by the 2 index entropy method. Examples of application for cracks obtained with relatively large voxel sizes (allowing scan times of the order of 30 minutes) have been shown for two different alloys.

In the case of synchrotron tomography, the thresholding process is made more complex by the coherence of the X-ray beam which produces diffraction effects and artifact at the crack edges. A reliable segmentation of such images normally involves a lot of human intervention and can hardly be automatic. We have proposed a deep learning method which uses a U-net network to replace human intervention during thresholding. By manually segmenting a limited amount of images (less than 2%) the software can be efficiently trained to detect internal cracks in a cast Al alloy. The probability map obtained from the neural network is thresholded using the algorithm developed for laboratory CT images. Finally, without supplementary training, 3D images of the propagation of a crack acquired during an *in situ* fatigue test have been successfully thresholded, showing the possibility to automatize the process. The same network was used successfully on a data-set obtained at a different synchrotron with different imaging and reconstruction conditions.

References

- 445 [1] J. Y. Buffiere, E. Maire, J. Adrien, J. P. Masse, E. Boller, In Situ Experiments with X ray Tomography: an Attractive Tool for Experimental Mechanics, *Experimental Mechanics* 50 (3) (2010) 289–305.
- [2] L. Salvo, P. Cloetens, E. Maire, S. Zabler, J. J. Blandin, J. Y. Buffière, W. Ludwig, E. Boller, D. Bellet, C. Josserond, X-ray micro-tomography an
450 attractive characterisation technique in materials science, *Nuclear Instruments and Methods in Physics Research Section B: Beam Interactions with Materials and Atoms* 200 (2003) 273–286.
- [3] E. Maire, J. Y. Buffière, L. Salvo, J. J. Blandin, W. Ludwig, J. M. Létang, On the Application of X-ray Microtomography in the Field of Materials
455 Science, *Advanced Engineering Materials* 3 (8) (2001) 539–546.
- [4] H. Toda, I. Sinclair, J.-Y. Buffière, E. Maire, T. Connolley, M. Joyce, K. H. Khor, P. Gregson, Assessment of the fatigue crack closure phenomenon in damage-tolerant aluminium alloy by in-situ high-resolution synchrotron X-ray microtomography, *Philosophical Magazine* 83 (21) (2003) 2429–2448.
- 460 [5] E. Maire, O. Bouaziz, M. Di Michiel, C. Verdu, Initiation and growth of damage in a dual-phase steel observed by X-ray microtomography, *Acta Materialia* 56 (18) (2008) 4954–4964.
- [6] S. Biroasca, J. Y. Buffiere, M. Karadge, M. Preuss, 3-D observations of short fatigue crack interaction with lamellar and duplex microstructures
465 in a two-phase titanium alloy, *Acta Materialia* 59 (4) (2011) 1510–1522.
- [7] A. King, W. Ludwig, M. Herbig, J. Y. Buffière, A. A. Khan, N. Stevens, T. J. Marrow, Three-dimensional in situ observations of short fatigue crack growth in magnesium, *Acta Materialia* 59 (17) (2011) 6761–6771.
- [8] S. C. Wu, T. Q. Xiao, P. J. Withers, The imaging of failure in structural
470 materials by synchrotron radiation X-ray microtomography, *Engineering Fracture Mechanics* 182 (2017) 127–156.

- [9] S. D. Yanowitz, A. M. Bruckstein, A new method for image segmentation, *Computer Vision, Graphics, and Image Processing* 46 (1) (1989) 82–95.
- [10] U. K. Bhowmik, D. Mandala, N. W. Hudyma, O. P. Kreidl, A. Harris, Segmentation of cracks in X-ray CT images of tested macroporous plaster specimens, in: *IEEE SOUTHEASTCON 2014*, 2014, pp. 1–8, iSSN: 1558-058X, 1091-0050.
- [11] O. Tankyevych, H. Talbot, P. Dokladál, N. Passat, Spatially-Variant Morpho-Hessian Filter: Efficient Implementation and Application, in: M. H. F. Wilkinson, J. B. T. M. Roerdink (Eds.), *Mathematical Morphology and Its Application to Signal and Image Processing*, Computer Science, Lecture Notes, Springer, Berlin, Heidelberg, 2009, pp. 137–148.
- [12] A. Larrue, A. Rattner, Z.-A. Peter, C. Olivier, N. Laroche, L. Vico, F. Peyrin, Synchrotron Radiation Micro-CT at the Micrometer Scale for the Analysis of the Three-Dimensional Morphology of Microcracks in Human Trabecular Bone, *PLOS ONE* 6 (7) (2011) e21297.
- [13] U. Wolfram, J. Schwiedrzik, M. Mirzaali, A. Bürki, P. Varga, C. Olivier, F. Peyrin, P. Zysset, Characterizing microcrack orientation distribution functions in osteonal bone samples, *Journal of Microscopy* 264 (3) (2016) 268–281.
- [14] H. Oliveira, P. L. Correia, CrackIT — An image processing toolbox for crack detection and characterization, in: *2014 IEEE International Conference on Image Processing (ICIP)*, 2014, pp. 798–802, iSSN: 1522-4880, 2381-8549.
- [15] Y. Shi, L. Cui, Z. Qi, F. Meng, Z. Chen, Automatic Road Crack Detection Using Random Structured Forests, *IEEE Transactions on Intelligent Transportation Systems* 17 (12) (2016) 3434–3445.
- [16] O. Çiçek, A. Abdulkadir, S. S. Lienkamp, T. Brox, O. Ronneberger, 3D U-Net: Learning Dense Volumetric Segmentation from Sparse Annotation,

- 500 in: S. Ourselin, L. Joskowicz, M. R. Sabuncu, G. Unal, W. Wells (Eds.),
Medical Image Computing and Computer-Assisted Intervention – MICCAI
2016, Springer International Publishing, Cham, 2016, pp. 424–432.
- [17] O. Ronneberger, P. Fischer, T. Brox, U-Net: Convolutional Networks for
Biomedical Image Segmentation, in: N. Navab, J. Hornegger, W. M. Wells,
505 A. F. Frangi (Eds.), Medical Image Computing and Computer-Assisted
Intervention – MICCAI 2015, Computer Science, Lecture Notes, Springer
International Publishing, Cham, 2015, pp. 234–241.
- [18] J. Shao, D. Du, X. Zhu, L. Wang, Weld Slim Line Defects Extraction Based
on Adaptive Local Threshold and Modified Hough Transform, in: 2009 2nd
510 International Congress on Image and Signal Processing, 2009, pp. 1–5.
- [19] Z. Li, L. Zeng, X. Zou, C. Xiang, Crack surface extraction of industrial
CT volume data using FPIT and planelet, Journal of X-Ray Science and
Technology 19 (1) (2011) 1–12.
- [20] M. Voorn, U. Exner, A. Rath, Multiscale Hessian fracture filtering for the
515 enhancement and segmentation of narrow fractures in 3D image data, Com-
puters & Geosciences 57 (2013) 44–53.
- [21] C. Chateau, T. T. Nguyen, M. Bornert, J. Yvonnet, DVC-based image
subtraction to detect microcracking in lightweight concrete, Strain 54 (5)
(2018) e12276.
- 520 [22] T. Strohmamm, K. Bugelnig, E. Breitbarth, F. Wilde, T. Steffens, H. Ger-
mann, G. Requena, Semantic segmentation of synchrotron tomography of
multiphase Al-Si alloys using a convolutional neural network with a pixel-
wise weighted loss function, Scientific Reports 9 (1) (2019) 1–9.
- [23] Y. Fujita, Y. Hamamoto, A robust automatic crack detection method from
525 noisy concrete surfaces, Machine Vision and Applications 22 (2) (2011)
245–254.

- [24] C. Tomasi, R. Manduchi, Bilateral filtering for gray and color images, in: Sixth International Conference on Computer Vision (IEEE Cat. No.98CH36271), Narosa Publishing House, Bombay, India, 1998, pp. 839–846.
- [25] F. Aguet, M. Jacob, M. Unser, Three-dimensional feature detection using optimal steerable filters, in: IEEE International Conference on Image Processing 2005, Vol. 2, 2005, pp. II–1158, ISSN: 1522-4880, 2381-8549.
- [26] A. Pacureanu, A. Larrue, M. Langer, C. Olivier, C. Muller, M. H. Lafage-Proust, F. Peyrin, Adaptive filtering for enhancement of the osteocyte cell network in 3D microtomography images, IRBM 34 (1) (2013) 48–52.
URL <http://www.sciencedirect.com/science/article/pii/S1959031812001492>
- [27] S. Lou, X. Jiang, P. J. Scott, Application of the morphological alpha shape method to the extraction of topographical features from engineering surfaces, Measurement 46 (2) (2013) 1002–1008.
- [28] H. Edelsbrunner, E. P. Mücke, Three-dimensional alpha shapes, ACM Transactions on Graphics 13 (1) (1994) 43–72.
- [29] P. Cloetens, M. Pateyron-Salomé, J. Y. Buffière, G. Peix, J. Baruchel, F. Peyrin, M. Schlenker, Observation of microstructure and damage in materials by phase sensitive radiography and tomography, Journal of Applied Physics 81 (9) (1997) 5878.
- [30] H. K. Danielsen, A. J. Carrasco, S. Fæster, K. V. Dahl, F. G. Guzmán, P. Sauvage, G. Jacobs, 3D X-ray computerized tomography of White Etching Cracks (WEC), Materials Characterization 150 (2019) 78–87.
- [31] J. Y. Buffiere, E. Ferrie, H. Proudhon, W. Ludwig, Three-dimensional visualisation of fatigue cracks in metals using high resolution synchrotron X-ray micro-tomography, Materials Science and Technology 22 (9) (2006) 1019–1024.

- 555 [32] S. Fæster, H. K. Danielsen, X-ray tomography data of White Etching Cracks (WEC), *Data in Brief* 27 (2019) 104531.
- [33] A. Messenger, A. Junet, T. Palin-Luc, J.-Y. Buffiere, N. Saintier, N. Ranc, M. E. May, Y. Gaillard, A. King, A. Bonnin, Y. Nadot, In situ synchrotron ultrasonic fatigue testing device for 3D characterisation of internal crack initiation and growth, *Fatigue & Fracture of Engineering Materials & Structures* 43 (3) (2020) 558–567.
- 560 [34] I. Serrano-Munoz, J. Y. Buffiere, C. Verdu, Y. Gaillard, P. Mu, Y. Nadot, Influence of surface and internal casting defects on the fatigue behaviour of A357-T6 cast aluminium alloy, *International Journal of Fatigue* 82 (2016) 361–370.
- 565 [35] F. P. Vidal, J. M. Létang, G. Peix, P. Cloetens, Investigation of artefact sources in synchrotron microtomography via virtual X-ray imaging, *Nuclear Instruments and Methods in Physics Research Section B: Beam Interactions with Materials and Atoms* 234 (3) (2005) 333–348.
- 570 [36] L. C. P. Croton, K. S. Morgan, D. M. Paganin, L. T. Kerr, M. J. Wallace, K. J. Crossley, S. L. Miller, N. Yagi, K. Uesugi, S. B. Hooper, M. J. Kitchen, In situ phase contrast X-ray brain CT, *Scientific Reports* 8 (1) (2018) 1–12.
- [37] C. Madonna, B. Quintal, M. Frehner, B. S. G. Almqvist, N. Tisato, M. Pistone, F. Marone, E. H. Saenger, Synchrotron-based X-ray tomographic microscopy for rock physics investigationsSynchrotron-based rock images, *Geophysics* 78 (1) (2013) D53–D64.
- 575 [38] J. Chen, L. Yang, Y. Zhang, M. Alber, D. Z. Chen, Combining Fully Convolutional and Recurrent Neural Networks for 3D Biomedical Image Segmentation, *arXiv:1609.01006 [cs]*ArXiv: 1609.01006.
- 580 [39] J. Jiang, X. Liu, L. Liu, S. Wang, E. Long, H. Yang, F. Yuan, D. yu, K. Zhang, L. Wang, Z. Liu, D. Wang, X. Changzun, Z. Lin, X. Wu, J. Cui, M. Zhu, H. Lin, Predicting the progression of ophthalmic disease based on

slit-lamp images using a deep temporal sequence network, PLOS ONE 13 (2018) e0201142.

585 [40] D. Paganin, S. C. Mayo, T. E. Gureyev, P. R. Miller, S. W. Wilkins, Simultaneous phase and amplitude extraction from a single defocused image of a homogeneous object, *Journal of Microscopy* 206 (1) (2002) 33–40.

[41] S. Irvine, R. Mokso, P. Modregger, Z. Wang, F. Marone, M. Stampanoni, Simple merging technique for improving resolution in qualitative single image phase contrast tomography, *Optics Express* 22 (22) (2014) 27257–27269.
590

5. Acknowledgements

The 3D images of the Al alloy sample shown in this work have been obtained within the GIGADEF project grant number ANR-16-CE08-0039. The authors thank the French National Research Agency for its financial support.
595 We acknowledge the Elettra and Soleil synchrotrons for provision of beamtime respectively at beamline SYRMEP (Dr.L.Mancini) and PSICHE (Dr.A.King). All members of the GIGADEF project are thanked for fruitful and lively discussions. C.Xiao is supported by a Grant obtained in the Cleansky project IDERPLANE (Contract number CE:821315). The bearing steel sample has
600 been provided by Prof. A.Mazzu from Brescia Univ.

Appendix A. Segmentation Parameters

Table A.1: Parameters used for crack segmentation. In the first row of the table: ‘Tomo lab’=volume obtained by laboratory CT, ‘Tomo syn’=volume obtained by Synchrotron CT.

Step	Variable	ER7(Tomo lab)	Al(Tomo lab)	Al(Tomo syn Soleil)	Al(Tomo syn Eltra)
Subtract filter	window size(voxel)	11×11×11	11×11×11	None	None
Linear bilateral filter	window size(voxel)	5×5×5	5×5×5	5×5×5	5×5×5
Linear bilateral filter	σ_{d1}	3	3	2	2
Linear bilateral filter	σ_{d2}	0.3	0.3	0.2	0.2
Steerable filter	window size(voxel)	3×3×3	5×5×5	3×3×3	3×3×3
Nonlinear bilateral filter	window size(voxel)	5×5×5	5×5×5	5×5×5	5×5×5
Nonlinear bilateral filter	σ_{d1}	3	3	3	3
Nonlinear bilateral filter	σ_{d2}	0.3	0.3	0.3	0.3
2index maxentropy threshold	α	0.3	0.3	0.2	0.2
2index maxentropy threshold	β	0.3	0.4	0.2	0.2
Unet	Learning rate	None	None	0.00001	0.00005
Unet	Type of loss function	None	None	Cross entropy	Cross entropy

Appendix B. Details about U-net

Table B.2: Detailed operations and parameters in the construction of the used U-net network

Step number	Operation number	Operation name	Parameters
Step 1	Operation 1	Conv2D	Kernel size=(3,3), filters number=64, activation function=Relu, Padding=1
Step 1	Operation 2	Conv2D	Kernel size=(3,3), filters number=64, activation function=Relu, Padding=1
Step 1	Operation 3	MaxPooling2D	Pool size=(2,2)
Step 2	Operation 1	Conv2D	Kernel size=(3,3), filters number=128, activation function=Relu, Padding=1
Step 2	Operation 2	Conv2D	Kernel size=(3,3), filters number=128, activation function=Relu, Padding=1
Step 2	Operation 3	MaxPooling2D	Pool size=(2,2)
Step 3	Operation 1	Conv2D	Kernel size=(3,3), filters number=256, activation function=Relu, Padding=1
Step 3	Operation 2	Conv2D	Kernel size=(3,3), filters number=256, activation function=Relu, Padding=1
Step 3	Operation 3	MaxPooling2D	Pool size=(2,2)
Step 4	Operation 1	Conv2D	Kernel size=(3,3), filters number=512, activation function=Relu, Padding=1
Step 4	Operation 2	Conv2D	Kernel size=(3,3), filters number=512, activation function=Relu, Padding=1
Step 4	Operation 3	MaxPooling2D	Pool size=(2,2)
Step 5	Operation 1	Conv2D	Kernel size=(3,3), filters number=1024, activation function=Relu, Padding=1
Step 5	Operation 2	Conv2D	Kernel size=(3,3), filters number=1024, activation function=Relu, Padding=1
Step 5	Operation 3	Dropout	Rate=0.33
Step 6	Operation 1	UpSampling2D	Magnification=(2,2), Method=Bilinear interpolation
Step 6	Operation 2	Concatenate	input=(output of Step 6.1, output of Step 4.2)
Step 6	Operation 3	Conv2D	Kernel size=(3,3), filters number=512, activation function=Relu, Padding=1
Step 6	Operation 4	Conv2D	Kernel size=(3,3), filters number=512, activation function=Relu, Padding=1
Step 7	Operation 1	UpSampling2D	Magnification=(2,2), Method=Bilinear interpolation
Step 7	Operation 2	Concatenate	input=(output of Step 7.1, output of Step 3.2)
Step 7	Operation 3	Conv2D	Kernel size=(3,3), filters number=256, activation function=Relu, Padding=1
Step 7	Operation 4	Conv2D	Kernel size=(3,3), filters number=256, activation function=Relu, Padding=1
Step 8	Operation 1	UpSampling2D	Magnification=(2,2), Method=Bilinear interpolation
Step 8	Operation 2	Concatenate	input=(output of Step 8.1, output of Step 2.2)
Step 8	Operation 3	Conv2D	Kernel size=(3,3), filters number=128, activation function=Relu, Padding=1
Step 8	Operation 4	Conv2D	Kernel size=(3,3), filters number=128, activation function=Relu, Padding=1
Step 9	Operation 1	UpSampling2D	Magnification=(2,2), Method=Bilinear interpolation
Step 9	Operation 2	Concatenate	input=(output of Step 9.1, output of Step 1.2)
Step 9	Operation 3	Conv2D	Kernel size=(3,3), filters number=64, activation function=Relu, Padding=1
Step 9	Operation 4	Conv2D	Kernel size=(3,3), filters number=64, activation function=Relu, Padding=1
Step 10	Operation 1	Conv2D	Kernel size=(3,3), filters number=2, activation function=Relu, Padding=1
Step 10	Operation 2	Conv2D	Kernel size=(1,1), filters number=1, activation function=Sigmoid, Padding=0

Table B.3: Explanation list of technical terms using in Deep Learning, more details can be found in [22] [17]

Conv2D	A 2D Convolution operation, which uses K convolution kernels (size: $N \times N$) which are applied to the input image to produce K new images (called feature maps). The feature maps size is the same as input image (while preserving the edges, a process called padding).
Relu	(rectified linear activation function) is a linear function that will output the input directly if it is positive, otherwise, it will output zero. It has become the default activation function for many types of neural networks because a model that uses it is easier to train and often achieves better performance.
MaxPooling2D	A 2D down-sample operation, which takes the maximum value within a $M \times M$ window and outputs a smaller image (generally half size).
Upsampling2D	A 2D upsample operation, which uses bilinear interpolation to increase the input image size.
Dropout	The Dropout layer randomly sets input units to 0 with a frequency of rate, which helps prevent overfitting. Inputs not set to 0 are scaled up by $1/(1 - \text{rate})$ such that the sum over all inputs is unchanged (0.33 and 0.5 are the commonly used empirical values of rate).
Concatenate	Two batches of feature maps of the same size (one obtained during Encoding and one obtained during Decoding) are stacked together and the channel of output is equal to their sum.
Softmax	(normalized exponential function) produces a probability distribution of values between 0 and 1 from the last step of the network.

Appendix C. Laboratory tomography: segmentation of a fatigue crack in a cast Al alloy

605 A fatigue crack initiated from an artificial surface defect during ultrasonic fatigue has been observed in a cast Al sample by laboratory tomography. Because of the sample size (3mm) a relatively large voxel size had to be used (2.5 μm) resulting in a very low contrast for the crack (Figure C.10). In spite of those difficult conditions the crack could be successfully segmented by the segmentation method described in this work (section 2.1). The total segmentation time is 2 hours.

610

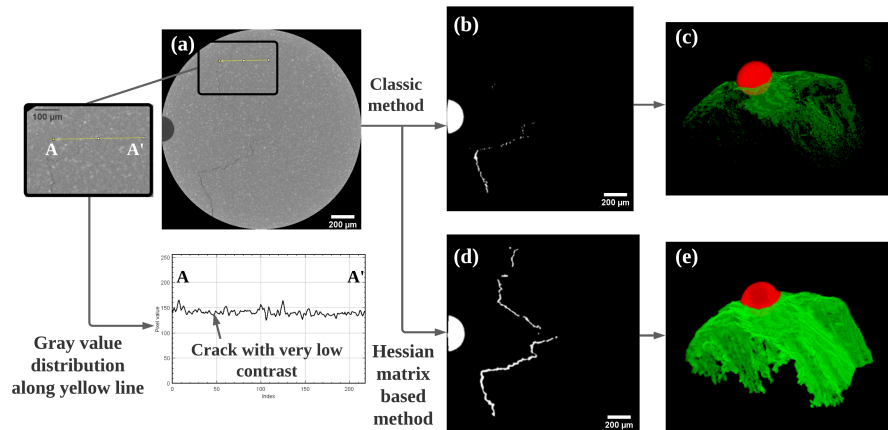


Figure C.10: Segmentation of a fatigue crack observed by laboratory CT in a cast Al sample. (a) 2D reconstructed slice (voxel size =2.5 μm) because of the small opening (unloaded sample) the crack contrast within the Al matrix is very weak. (b) and (c) Segmented slice and 3D rendering obtained by classical gray level histogram threshold (d) and (e) Segmented slice and 3D rendering obtained by the Hessian matrix-based method. The Hessian matrix improves the continuity of the binary crack in spite of its low contrast and opening. In the 3D rendering, the artificial hemispheric surface defect located on the surface is shown in red. Sample diameter 3mm, voxel size 2.5 μm , Accel. voltage 160 kV, scanning time 30 minutes.

Appendix D. Effect of loss function and learning rates

A range of parameters and functions can be used to tune the Unet network. In this work, as a first approach, we have investigated the number of images composing the ground truth, two loss functions and two learning rates. The results obtained by varying the number of images have been shown in section 3.2.4, in this part we summarize the comparison of results obtained with two loss functions and learning rates. The two tested loss functions are the *dice loss* and the *binary cross-entropy*. As shown in Figure D.11, at the same learning rate (1×10^{-5}), with ‘dice loss’ the Unet model converges faster than with ‘cross-entropy’, but the former ends up with a higher loss: 0.2 against 0.1 for cross-entropy. The same trend is observed on the validation images. Moreover, the predicted image obtained using cross-entropy appears closer to Ground truth than when dice-loss is used.

Two different learning rates have been tested. As shown in Figure D.12.h and .g, the predicted image obtained with ‘learning rate= 1×10^{-5} ’ has less noise than the one trained with ‘learning rate= 1×10^{-4} ’ and was selected.

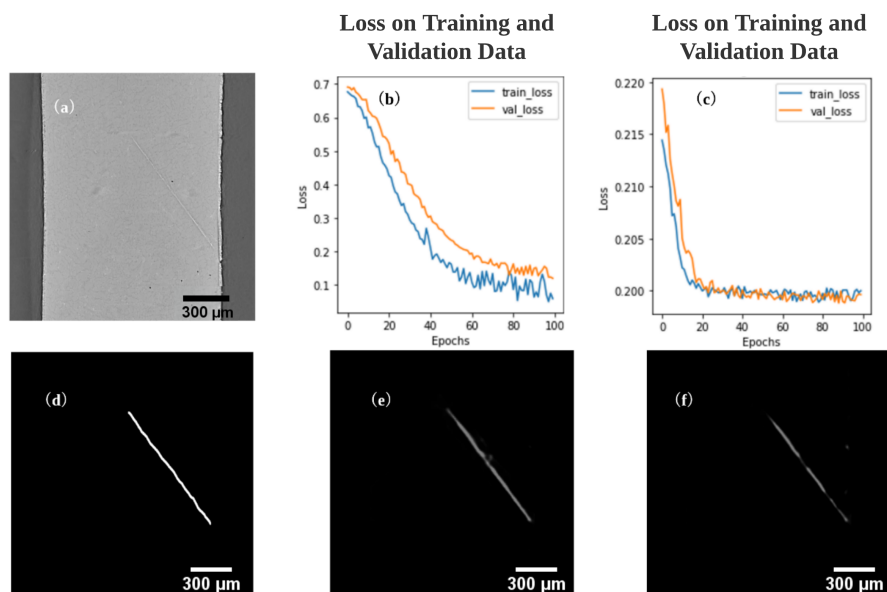


Figure D.11: Effect of loss function on predicted image. (a) test image. Loss evolution during training for 'cross-entropy' (b) and 'Dice loss' (c) (d) Ground Truth of test image. (e) Probability map of test image obtained with 'cross-entropy'; (f) Probability map of test image obtained with 'dice-loss'

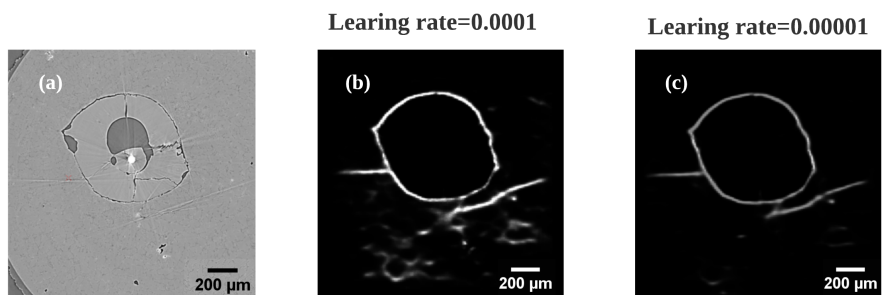


Figure D.12: Effect of learning rates on predicted image. (a) 2D test image. (b) Probability map obtained with 'learning rate= 1×10^{-4} ' (c) 'learning rate= 1×10^{-5} '.